ISSN 1027-4510, Journal of Surface Investigation. X-ray, Synchrotron and Neutron Techniques, 2015, Vol. 9, No. 1, pp. 44–52. © Pleiades Publishing, Ltd., 2015.
Original Russian Text © G.D. Bokuchava, I.V. Papushkin, V.I. Bobrovskii, N.V. Kataeva, 2015, published in Poverkhnost'. Rentgenovskie, Sinkhrotronnye i Neitronnye Issledovaniya, 2015, No. 1, pp. 49–57.

Evolution in the Dislocation Structure of Austenitic 16Cr–15Ni–3Mo–1Ti Steel Depending on the Degree of Cold Plastic Deformation

G. D. Bokuchava[a], I. V. Papushkin[a], V. I. Bobrovskii[b], and N. V. Kataeva[b]

[a] *Frank Laboratory of Neutron Physics, Joint Institute for Nuclear Research, Dubna, Moscow oblast, 141980 Russia*

[b] *Institute of Metal Physics, Ural Branch, Russian Academy of Sciences, Yekaterinburg, 620990 Russia*

e-mail: gizo@nf.jinr.ru

Received April 22, 2014

Abstract—High-resolution neutron diffraction is employed to determine the main structural parameters and microstrain levels of several austenitic 16Cr–15Ni–3Mo–1Ti steel samples subjected to different degrees of cold plastic deformation and estimate the dislocation densities thereof. It is demonstrated that the anisotropic diffraction peak broadening observed in the neutron experiment is caused by variations in the dislocation-contrast factor and can be satisfactorily described with the help of the used model. Comparative analysis of the results obtained by neutron diffraction and transmission electron microscopy is performed.

Keywords: austenitic steel, cold deformation, dislocation structure, neutron diffraction, transmission electron microscopy

DOI: 10.1134/S1027451015010048

INTRODUCTION

During operation, constructional materials of nuclear reactors are exposed to fast-neutron fluxes. An increase in the reliability, safety, and cost effectiveness of reactors imposes higher requirements on their radiation resistance. At present, special austenitic stainless steels, which are very complicated objects to study the radiation behavior thereof, are widely applicable as the aforementioned materials. They are characterized by multiple components of chemical composition, a great variety of phases, and dependence of their properties on the treatment technology and operating conditions. Radiation processes occur in both the intrinsic matrix structures of these materials and impurities of other phases. The action of fast neutrons leads to the precipitation and dissolution of new phases, the coalescence of precipitated substances, and, on the contrary, their grain refinement, pore formation, and radiation-induced swelling. In investigating reactor materials subjected to radiation exposure, the features of the real crystalline structure thereof, which are connected with the manufacturing technique, must also be taken into account, such as texture, internal stresses, and interactions of the latter with radiation-induced defects.

It is known that nanosystems composed of intermetallic or carbide compounds formed due to the artificial ageing of materials exert a significant influence on their behavior under irradiation. Neutron-diffraction studies into the intermetallic and carbide ageing of austenitic 26Ni–5Cr–3Ti and 0.40C–4Cr–18Mn–2V steels were performed in [1, 2]. However, as was established by studying neutron-irradiation effects in pure nickel [3], the development of radiation damages of face-centered cubic (fcc) metals can also depend on the dislocation system formed by mechanical deformation. Thus, to investigate how the intrinsic mechanical treatment of austenitic steels affects the irradiation-initiated behavior, 16Cr–15Ni–3Mo–1Ti steel with a low titanium content was chosen and used to prepare samples whose degrees of cold deformation were 10, 20, 30, and 40%. First, it was ascertained that, in the former steel, an intermetallic Ni_3Ti phase is barely segregated in the initial unaged state and its clusters appear only upon annealing at ~600°C. Second, in contrast, e.g., to titanium-enriched 26Ni–5Cr–3Ti steel samples, the neutron-diffraction patterns of the given material have no additional reflections after its irradiation with fast neutrons. During the first stage, the unirradiated samples mentioned above were studied to estimate the neutron diffraction applicability to solving this problem and acquire initial data of the analysis of radiation-induced defects. During subsequent neutron-diffraction investigations of the irradiated samples, these data can serve as reference information.

RESOLUTION FUNCTION *R* OF THE TIME-OF-FLIGHT DIFFRACTOMETER

Neutron diffraction is to a large extent similar to X-ray scattering. However, unlike characteristic X-rays, slow neutrons possess a continuous (Max-

wellian) energy spectrum. In the experiment based on a pulsed source, the neutron energy can be analyzed via the time-of-flight (TOF) method because the slow neutron velocity is rather small. Depending on the wavelength, the diffraction-peak position on the time scale is determined from the condition

$$t = L/v = \lambda mL/h = 2mLd_{hkl}\sin\theta/h, \quad (1)$$

where L is the total flight distance between the neutron source and the detector; v, λ, and m designate, respectively, the velocity, wavelength, and mass of neutrons; h is Planck's constant; d_{hkl} is the interplanar spacing; and θ is the Bragg angle.

The resolution of the TOF neutron diffractometer is defined by the expression

$$R = \Delta d/d = [(\Delta t_0/t)^2 + (\Delta\theta/\tan\theta)^2 + (\Delta L/L)^2]^{1/2}, \quad (2)$$

where Δt_0 is the neutron-pulse width, $t = 252.778L\lambda$ is the total time of flight (in microseconds), L is the total flight distance between the source and the detector (in meters), λ is the neutron wavelength (in angstroms), and θ is the Bragg angle. The first term is the time component of the resolution function, i.e., a TOF uncertainty; the second is the geometric component of the resolution function, which characterizes all geometric uncertainties under scattering at different angles; and the third is a flight-distance uncertainty.

Thus, the instrument resolution is improved if the neutron-pulse width decreases and the flight distance or scattering angle increases. For neutron sources with a short neutron pulse (~20 μs/Å), the instrument resolution can attain ~10^{-3} at a substantially increased path length (~100 m) with a corresponding loss in intensity. For neutron sources (e.g., an IBR-2 fast pulsed reactor) with a long neutron pulse, such a method is unjustified. Hence, a special-purpose correlation technique is used to obtain high diffractometer resolution based on the given sources. In this case, at a comparatively short path length (~20 m), a multiple decrease in the effective pulse duration is achieved using a fast Fourier chopper, which modulates the primary neutron-beam intensity, in combination with the reverse TOF (RTOF) method for data acquisition [4].

In the RTOF method, the TOF diffraction spectrum is accumulated by continuously varying the Fourier chopper rotation speed according to a certain law (from zero to the maximum frequency Ω). In this case, the time component of the resolution function depends on the given frequency distribution $g(\omega)$ and the maximum rotation speed of the Fourier chopper and can be represented as

$$\Delta t/t_0 \sim \int_0^{\Omega} g(\omega)\cos(\omega t)d\omega, \quad (3)$$

where ω_{max} is the maximum rotation speed of the Fourier chopper, N is the number of slits in the Fourier chopper, and $\Omega = N\omega_{max}$ is the maximum modulation frequency of the neutron-beam intensity. Moreover, in contrast to a conventional TOF diffractometer whose pulse width depends linearly on the wavelength, the effective pulse width is constant and, to sufficient accuracy, is equal to the reciprocal value of the maximum modulation frequency in the given experiment. In other words,

$$\Delta t = \frac{1}{\Omega} = \frac{1}{N\omega_{max}}. \quad (4)$$

For a Fourier stress diffractometer (FSD), the maximum modulation frequency is Ω = 102.4 kHz and, accordingly, the effective pulse width is Δt = 9.77 μs at N = 1024 and ω_{max} = 6000 rpm. Thus, when the flight distance between a chopper and a detector is fairly short (~6.6 m) and the scattering angle is $2\theta = 90°$, the time-component contribution to the resolution function is $\Delta t_0/t \approx 2 \times 10^{-3}$ at d = 2 Å. The geometric contribution is commonly optimized by selecting the appropriate configuration of the detector system. In so doing, its value must be less than the time-component contribution to the total instrument resolution function.

As a rule, TOF diffractometers exhibit a rather wide range of interplanar spacings and, consequently, possess a large number of simultaneously observed diffraction peaks. In addition, the functional dependence between the diffraction-peak width and the interplanar spacing enables us to estimate microstrains and the size of coherent scattering regions on crystallites in a rather simple way:

$$\Delta d^2 = C_1 + C_2 d^2 + \langle\varepsilon^2\rangle d^2 + d^4/\langle D\rangle^2, \quad (5)$$

Here, Δd is the diffraction-peak width at half maxima; C_1 and C_2 are, respectively, the time and geometric components that define the diffractometer resolution function (their values are found from measurements with a standard sample); $\langle\varepsilon^2\rangle^{1/2} = (\Delta a/a)$ is the variance of the unit-cell parameter (microstrain); and $\langle D\rangle$ is the size of coherent scattering regions on crystallites.

Analysis of the shape of a diffraction peak (in the simplest case, its width) can provide data on crystal-lattice distortions (microstrains) inside individual grains and their sizes. A conventional approach developed primarily for X-ray diffraction is the harmonic analysis of several diffraction peaks corresponding to different orders of reflection from the same (*hkl*) plane [5]. Alternative techniques [6], which make it possible to remove restrictions inherent to classical harmonic analysis, have also been created recently. In addition, the authors of [7, 8] have developed methods for analyzing not only diffraction-peak shifts caused by oriented microstresses, but also a decrease in the diffraction-peak intensity and an increase in the diffuse background, which arise from statistical lattice distortions produced by atom shifts from ideal positions [9].

EXPERIMENT AND SAMPLES UNDER STUDY

The microstrains of the 16Cr–15Ni–3Mo–1Ti steel samples were experimentally studied using the FSD of the IBR-2 fast pulsed reactor situated at the

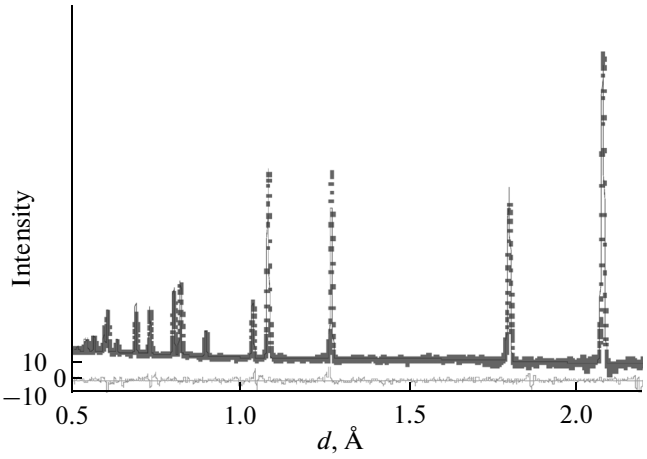

Fig. 1. Diffraction spectrum of the 16Cr–15Ni–3Mo–1Ti steel sample deformed by 20%. Data were measured using the FSD and processed by the Rietveld method. Experimental points and calculated and difference curves are shown.

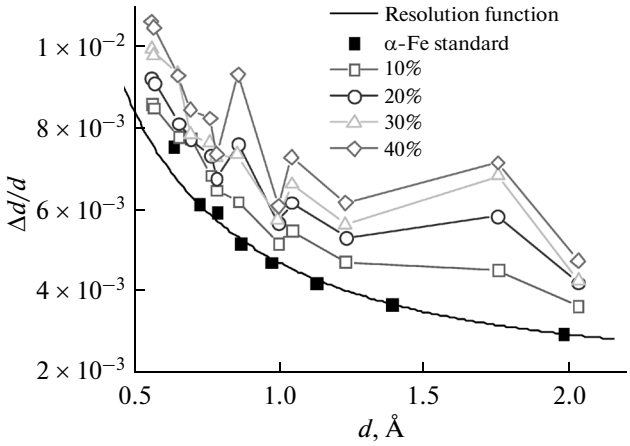

Fig. 2. Dependences between the full resolution function $\Delta d/d$ and the interplanar spacing d at different degrees of deformation of the steel samples under study. For comparison, the instrument resolution function measured with the help of the standard sample is shown.

Frank Laboratory of Neutron Physics, Joint Institute for Nuclear Research [10, 11], which was created to investigate internal mechanical stresses in industrial products and new promising materials via the Fourier correlation technique applied to neutron diffraction.

In this work, a set of four austenitic 16Cr–15Ni–3Mo–1Ti steel samples with degrees of cold deformation of 10, 20, 30, and 40% were examined. They were fabricated as cylinders 55 mm long and 6.45 mm in diameter. The diffraction spectra of the 16Cr–15Ni–3Mo–1Ti steel samples under study were measured at room temperature, and the exposure time of each spectrum was 2 h. All main diffraction peaks of the spectra were indicated in the scope of the fcc structure with the space group $Fm3m$ and the lattice constant $a_0 \approx 3.6$ Å. The typical diffraction spectrum processed by means of the Rietveld method is presented in Fig. 1. The main structural parameters were obtained using profile analysis of the measured diffraction spectra according to the Rietveld method. In addition, separate diffraction peaks were processed with the help of the least-squares (LS) method to analyze the dependence between the peak width and the interplanar spacing and to determine how crystal-lattice microstrains and the average size of coherent scattering crystallites contribute to the peak width.

RESULTS AND DISCUSSION

Neutron Diffraction

Analysis indicates that the dependence between the FSD resolution function and the interplanar spacing d is quite simple and that the instrument resolution increases gradually with spacing d. The FSD resolution function, as well as its sensitivity to the diffraction-peak broadening induced mainly by microstrains in the material and finite-size crystallites, was estimated at the preliminary stage. For this purpose, the diffraction spectrum of the standard α-Fe powder sample was measured. As is evident from Fig. 2, where the instrument resolution functions Δd measured with the help of the standard sample and the steel samples under study are compared, existing broadening effects can be reliably measured using the FSD.

When the diffraction-peak width at half maxima is analyzed with the aim of studying microstrains defined by formula (5), it is convenient to subtract the instrument resolution function and, afterward, examine the diffraction-peak broadening β related only to the properties of the material under consideration. Thus, for the investigated samples, analysis of the interrelation between peak broadening β^2 and d^2 revealed that certain ($h00$ and hhh) reflections deviate markedly from the linear dependence. Such a deviation is usually associated with variations in the dislocation-contrast factor and was observed more than once during X-ray scattering experiments [12, 13]. It should be noted that the anisotropic peak-broadening effect manifests itself very strongly with the use of the FSD (Fig. 3).

The study of diffraction-peak broadening demonstrated that crystallite sizes contribute negligibly to the broadening. On the contrary, microstrains make the main contribution to the above phenomenon. The crystal-lattice constant depends weakly on the degree of sample deformation, and its absolute value is in good agreement with our previous results obtained in studying the different heat-treatment modes of the same steel grade (see table) [14, 15]. At the same time, individual diffraction peaks of the spectrum become broader with increasing degree of deformation, as is

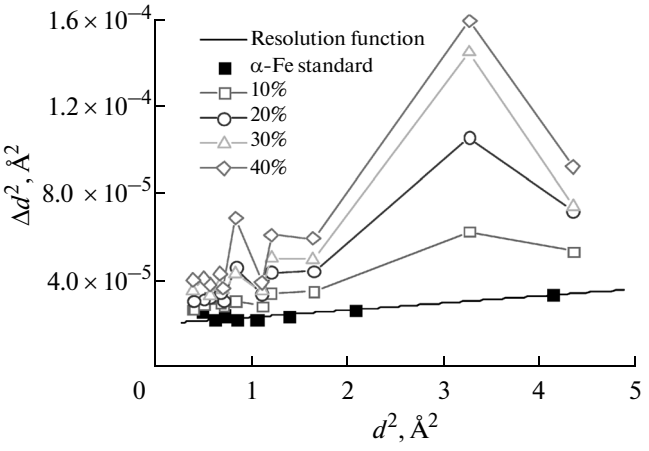

Fig. 3. Dependences between the squared peak half-width Δd^2 and the squared interplanar spacing d^2 of the investigated samples and the standard sample.

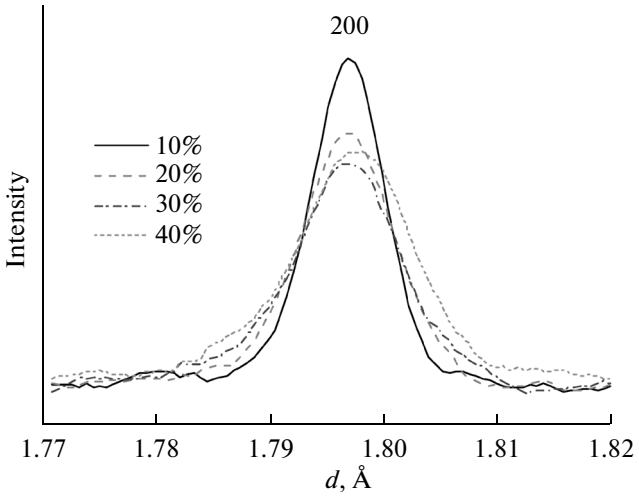

Fig. 4. Dependences between the (200) diffraction peak shape and the degree of plastic deformation of the 16Cr–15Ni–3Mo–1Ti steel samples.

seen in Fig. 4, confirming that material microstrains grow within very wide limits.

Microstrains $\langle\varepsilon^2\rangle^{1/2}$ and coherent-scattering-region sizes $\langle D\rangle$, which were obtained from analysis of the diffraction-peak broadening, can be employed to estimate an important parameter, namely, the dislocation density of the material under investigation. From comparison between the crystal lattice's elastic energy per unit volume and the energy of a single dislocation, it was demonstrated [16] that the dislocation density can be represented as

$$\rho = \frac{k}{F}\frac{\langle\varepsilon^2\rangle}{b^2}. \quad (6)$$

Here, $\langle\varepsilon^2\rangle^{1/2}$ is the microstrain; b is the Burgers vector; parameter F allows for the interaction of dislocations (in the simplest case, $F = 1$); and $k = 12A$, where $A = 2$ corresponds to the Lorentzian peak shape and $A = \pi/2$, to the Gaussian shape. As a rule, the coefficient k of many materials varies from 2 to 25. Moreover, with application of the given model, it is assumed that all dislocations contribute to diffraction-peak broadening and microstrains are independent of the [*hkl*] direction in the crystal. In particular, when the Burgers vector of dislocations is oriented along the [110] direction ($F = 1$), it was established that the dislocation density of the fcc lattice is defined as

$$\rho = 16.1\frac{\langle\varepsilon^2\rangle}{b^2}. \quad (7)$$

As was indicated above, the FSD spectra exhibit anisotropic diffraction-peak broadening associated with variations in the dislocation-contrast factor. The given anisotropic effect can be taken into account using the model for random-orientation polycrystalline materials with the cubic system [17]. In this model, the anisotropic diffraction-peak broadening depends on the average dislocation-contrast factor $\overline{C}_{hkl}$ allowing for the orientational and elastic properties of dislocations:

$$(\Delta K)^2 = \left(\frac{0.9}{\langle D\rangle}\right)^2 + \frac{\pi M^2 b^2 \rho}{2} K^2 C \pm O\left(K^4 C^2\right). \quad (8)$$

Crystal-lattice constants, average microstrains, and dislocation densities determined via neutron diffraction and TEM at different degrees of plastic deformation of 16Cr–15Ni–3Mo–1Ti steel

Degree of deformation, %	a, Å	$\varepsilon \times 10^{-4}$	Diffraction, $\rho \times 10^{14}$, m^{-2}	TEM, $\rho \times 10^{14}$, m^{-2}
10	3.59655 ± 0.00001	11.4 ± 0.1	1.7	3.0–5.0
20	3.59616 ± 0.00002	16.5 ± 0.1	3.9	4.0–5.0
30	3.59643 ± 0.00002	19.0 ± 0.2	5.8	4.5–6.0
40	3.59766 ± 0.00002	21.4 ± 0.2	6.9	8.0–10.0

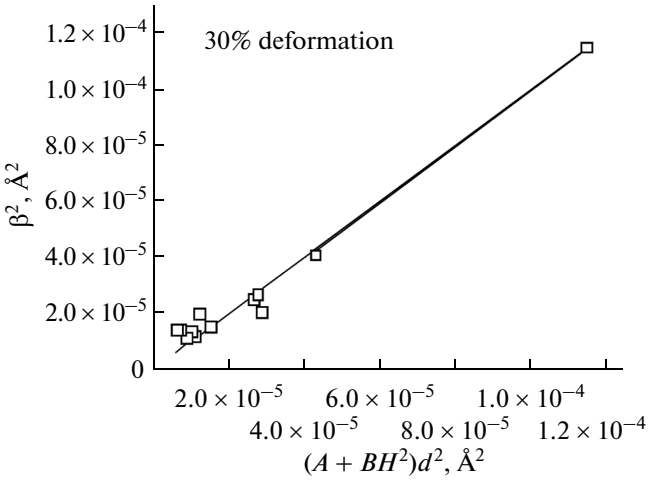

Fig. 5. Variations in the squared peak broadening β^2 vs. $(A + BH^2)d^2$ at 30% deformation of the sample. White squares designate experimental values, and the continuous line corresponds to the LS fitting.

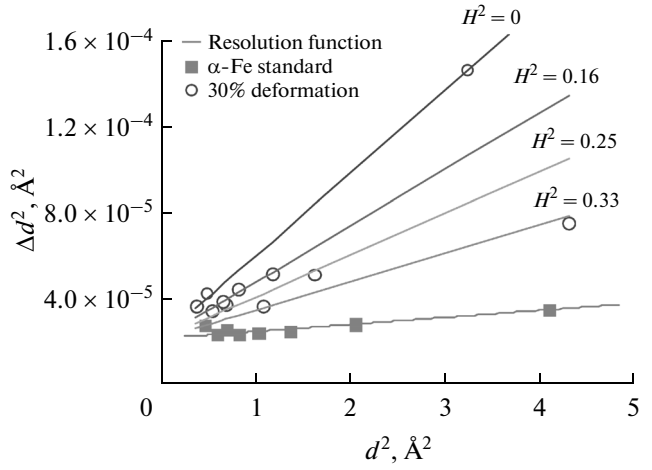

Fig. 6. Dependences between the squared peak half-width Δd^2 and the squared interplanar spacing d^2 at 30% deformation of the sample. The continuous lines were plotted using the LS fitting results and correspond to microstrains at different anisotropy factors H^2. For comparison, the instrument resolution function measured with the help of the standard sample is shown.

Here, $K = 2\sin\theta/\lambda$, ΔK is the peak width at half maxima, $\langle D\rangle$ is the coherent-scattering-region size, M is the constant determined by the effective radius of the dislocation cutoff, ρ is the dislocation density, b is the Burgers vector, C is the average dislocation-contrast factor, and $O(K^4C^2)$ are the higher-order residual terms.

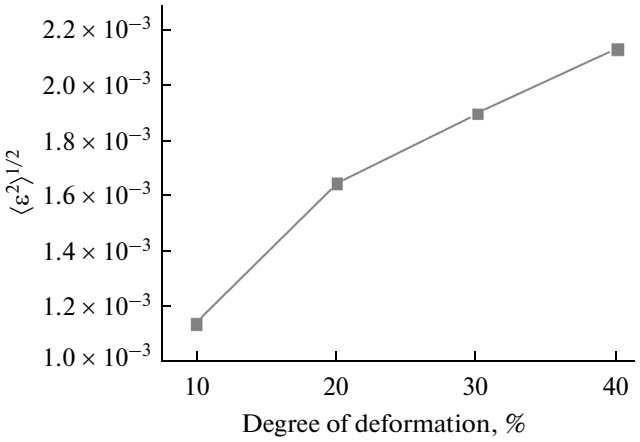

Fig. 7. Variations in the averaged lattice microstrain vs. the degree of plastic deformation of the material.

In particular, the averaged dislocation-contrast factor of a cubic crystal is described by the simple relationship

$$\overline{C}_{hkl} = A - B\frac{h^2k^2 + h^2l^2 + k^2l^2}{(h^2 + k^2 + l^2)^2} = A - BH^2, \qquad (9)$$

where h, k, and l are the Miller indices, H^2 is the orientation factor (anisotropy factor), and parameters A and B depend not only on the elastic constants of the material and the effective radius of the dislocation cutoff, but also on whether dislocations are of the edge or screw type. In this case, material microstrains are anisotropic and possess minimum and maximum values at $H^2 = 0$ and 0.33, respectively.

Thus, the given model based on LS fitting provides a satisfactory description of the anisotropic diffraction-peak broadening (Fig. 5). It should be emphasized that the parameters fitted via the LS method enable us to construct model curves corresponding to different values of the orientation factor H^2. In this case, the experimental values Δd^2 agree very well with the corresponding model curves (see Figs. 3, 6). The dependence of microstrains $\langle\varepsilon^2\rangle^{1/2}$, which is averaged over all orientations and corresponds to $H^2 = 0.2$, is depicted in Fig. 7. Its value increases if the degree of plastic deformation of the material increases. Accordingly, the dislocation density also increases from 1.7×10^{14} to 6.9×10^{14} m^{-2} (Fig. 8).

In addition, the aforementioned model can be used to estimate the ratio between edge or screw dislocations in the material under consideration. For this purpose, the experimentally determined dislocation-contrast factor $\overline{C}_{h00}$ must be compared with $\overline{C}^{\text{edge}}_{h00}$ and $\overline{C}^{\text{screw}}_{h00}$, i.e., with the separately calculated contrast factors of edge and screw dislocations, respectively. For

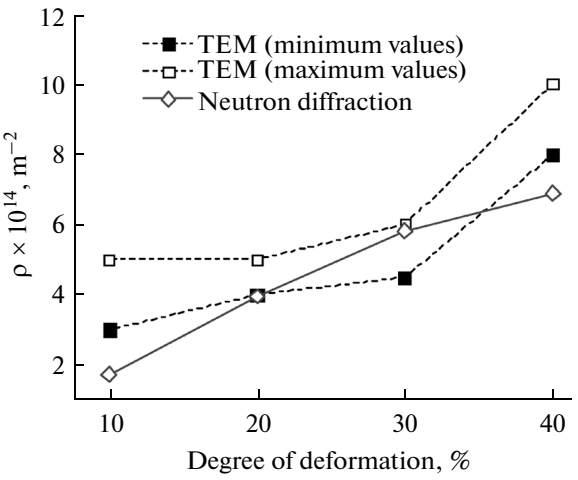

Fig. 8. Dependences between the dislocation density and the degree of plastic deformation of 16Cr–15Ni–3Mo–1Ti steel. The densities were measured via TEM (minimum and maximum values) and neutron diffraction.

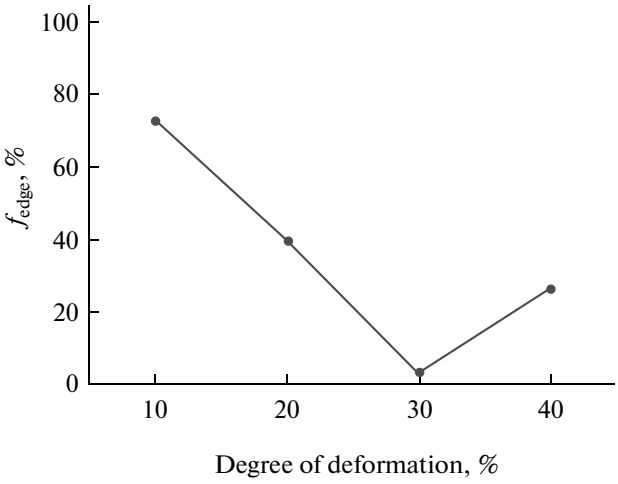

Fig. 9. Variations in the fraction of edge dislocations in the material vs. the degree of plastic deformation.

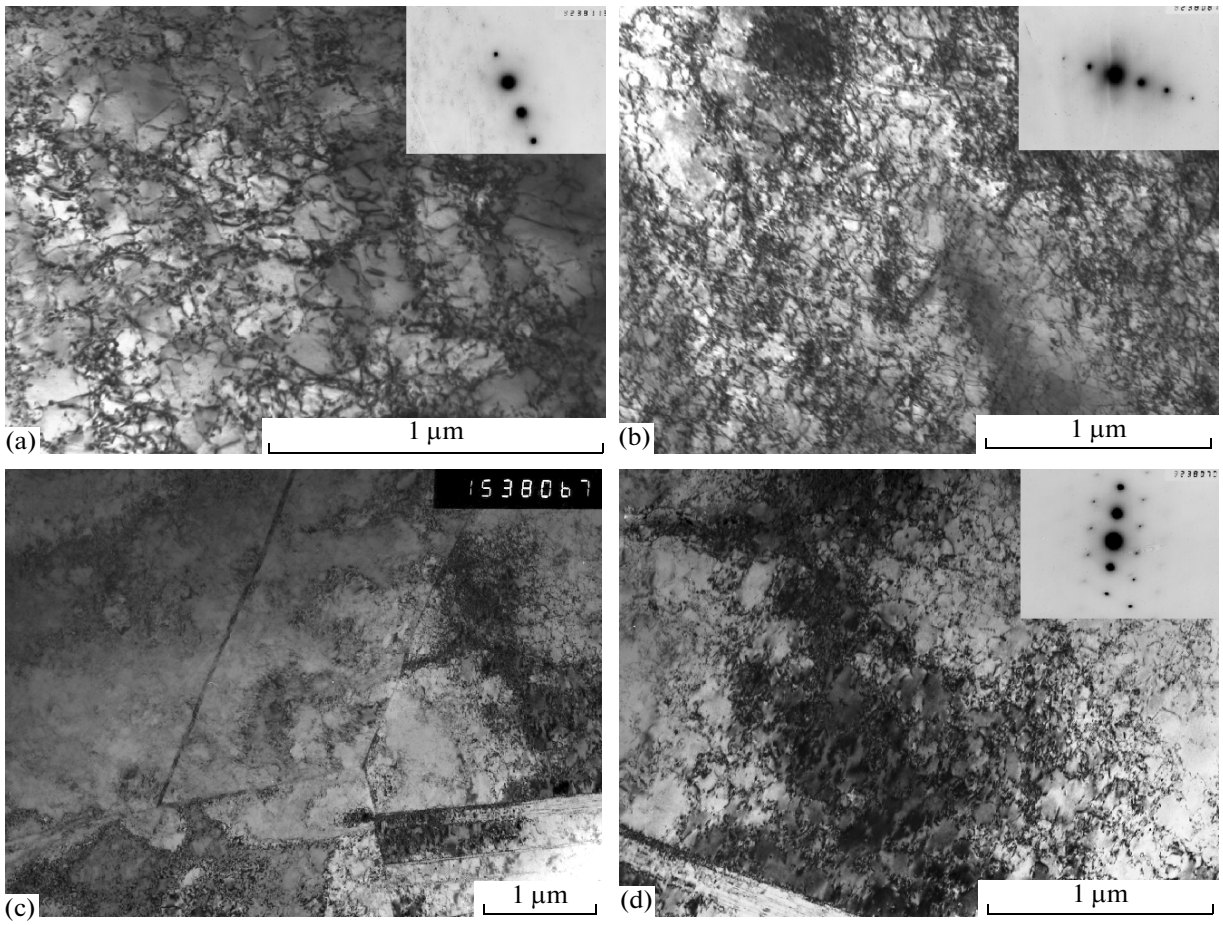

Fig. 10. Structures of 16Cr–15Ni–3Mo–1Ti steel deformed by (a, b) 10 and (c, d) 20%.

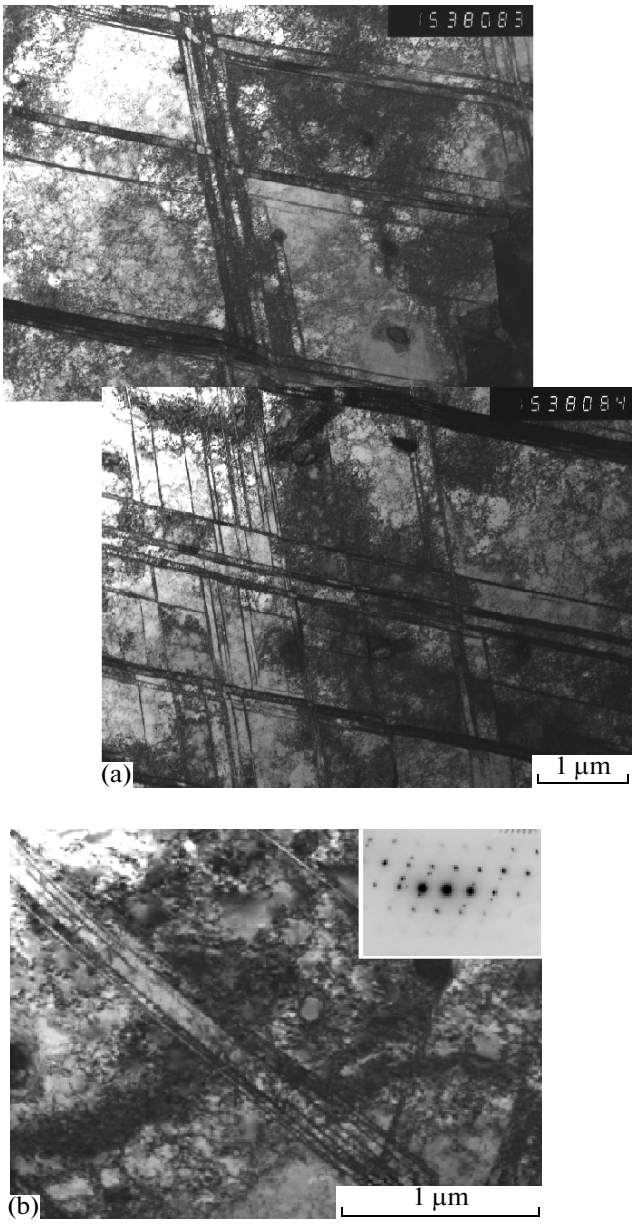

Fig. 11. Structures of 16Cr–15Ni–3Mo–1Ti steel deformed by (a, b) 30%.

16Cr–15Ni–3Mo–1Ti steel, the results are presented in Fig. 9. It is seen that, in the material investigated, the fraction of edge dislocations decreases from 75 to 4% with increasing degree of plastic deformation. (Accordingly, the fraction of screw dislocations increases under the same conditions.) Afterward, the fraction of edge dislocations increases and reaches 28% at the maximum degree of plastic deformation of 40%.

Transmission Electron Microscopy

Transmission electron microscopy (TEM) was also used to study variations in the dislocation structure versus the degree of sample deformation. TEM experiments were carried out using a JEM-200CX electron microscope operating at an accelerating voltage of 160 kV and specially prepared foils. The bright-field images of the structure, microdiffraction patterns, and the dark-field images of different reflections were obtained to identify phases. During foil preparation, the sample thickness was mechanically thinned to ~100 μm, followed by electropolishing in orthophosphoric acid mixed with chromic anhydride. The dislocation densities were determined by means of the secant method.

The structure of the examined steel samples deformed by 10 and 20% involves only single twins (Fig. 10). When the degrees of deformation of the material are 30 and 40%, the density of twins grows appreciably (Figs. 11, 12). During investigation of the structure of austenitic 16Cr–15Ni–3Mo–1Ti steel samples with different degrees of deformation, it was revealed that the dislocation density varies over the grain volume. There are regions with low and high dislocation densities. In all probability, this is explained by the fact that TEM is a local method employed to investigate separate regions of a thin foil, in which the dislocation density can vary substantially. As opposed to TEM, neutron-diffraction data are averaged over the entire volume of the sample under study and provide an integral estimate of the dislocation densities. Moreover, TEM results can be affected by dislocations that are formed on sample surfaces during thin foil preparation. Hence, the dislocation density in foils is smaller as compared to the initial material.

However, comparison between the findings of both methods indicates that, in our case, the dislocation-density estimates determined from the neutron-diffraction data coincide closely with the TEM results (see table, Fig. 8).

CONCLUSIONS

In this work, the main structural parameters, microstrain levels and dislocation-density estimates of austenitic 16Cr–15Ni–3Mo–1Ti steel samples with degrees of cold plastic deformation of 10, 20, 30, and 40% are determined by means of high-resolution neutron diffraction. It is demonstrated that the anisotropic diffraction-peak broadening observed in the neutron experiment arises from variations in the dislocation-contrast factor and can be satisfactorily described with the help of the used model. The dislocation-density estimates obtained via neutron diffraction and transmission electron microscopy are rather close to each other and agree well with the data determined for the given material in [18, 19].

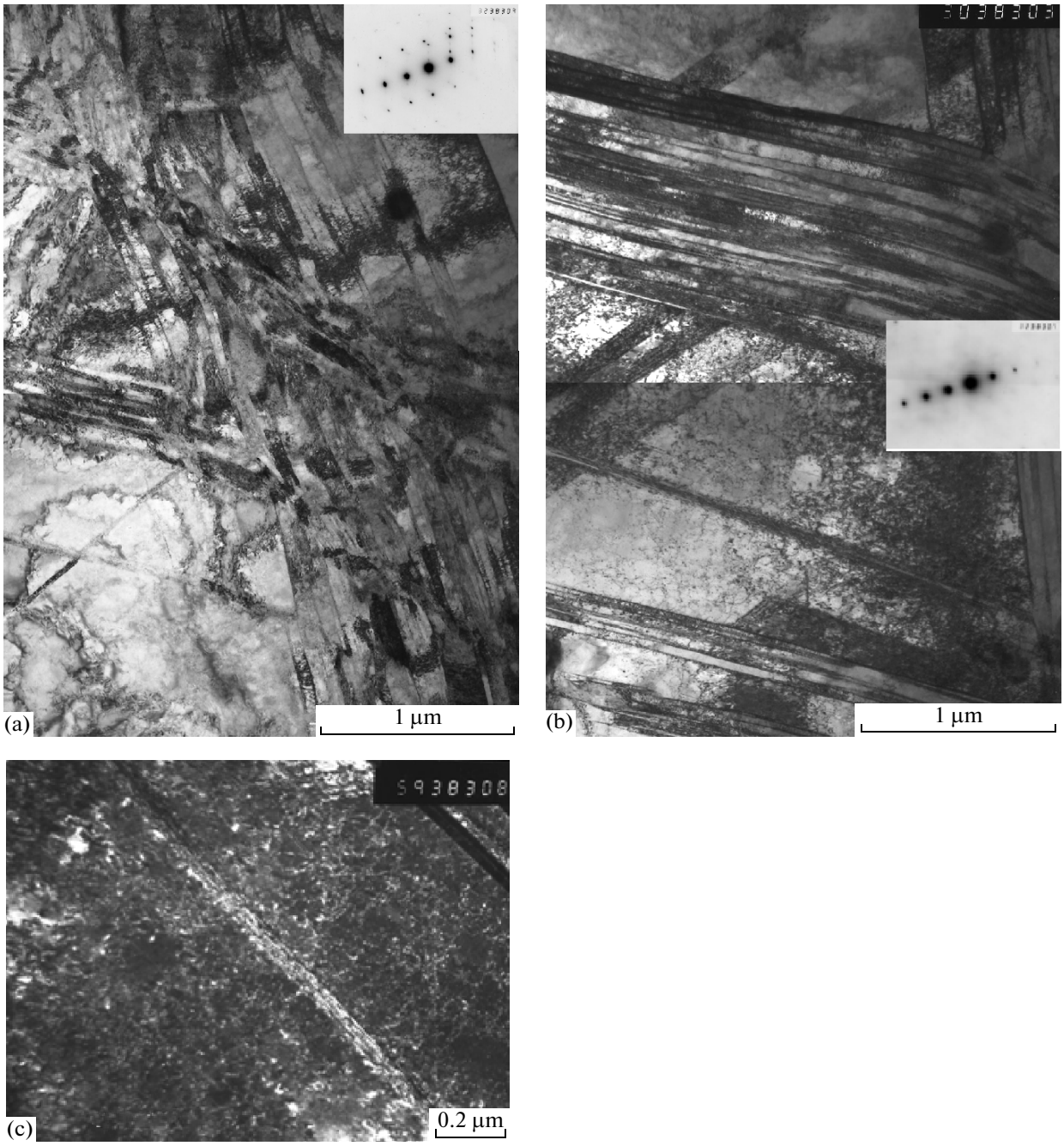

Fig. 12. Structures of 16Cr–15Ni–3Mo–1Ti steel deformed by (a, b) 40%: (a, b) bright-field images and (c) dark-field image of the $111_{\gamma.}$ reflection.

ACKNOWLEDGMENTS

We are grateful to A.M. Balagurov and V.V. Sumin for helpful discussions.

This work was supported in part by the Russian Foundation for Basic Research, project no. 12-02-12065-ofi_m.

REFERENCES

1. V. V. Sagaradze, V. I. Voronin, I. F. Berger, et al., Phys. Met. Metallogr. **112**, 517 (2011).
2. V. V. Sagaradze, B. N. Goshchitskii, E. G. Volkova, et al., Phys. Met. Metallogr. **111**, 80 (2011).
3. A. P. Druzhkov, D. A. Perminov, and V. L. Arbuzov, J. Nucl. Mater. **430**, 279 (2012).

4. P. Hiismaki, H. Poyry, and A. Tiitta, J. Appl. Crystallogr. **21**, 349 (1988).
5. B. E. Warren and B. L. Averbach, J. Appl. Phys. **2**, 595 (1950).
6. J. G. M. van Berkum, Ph.D. Thesis (Delft University of Technology, The Netherlands, 1994).
7. M. A. Krivoglaz, *X-ray and Neutron Diffraction in Nonideal Crystals* (Naukova Dumka, Kiev, 1983) [in Russian].
8. M. A. Krivoglaz, *Theory of X-ray and Thermal Neutron Scattering by Real Crystals* (Nauka, Moscow, 1967; Plenum Press, New York, 1969).
9. M. A. Krivoglaz, *Diffuse Scattering of X-Rays and Neutrons by Fluctuations* (Springer, New York, 1996).
10. G. D. Bokuchava, V. L. Aksenov, A. M. Balagurov, et al., Appl. Phys. A: Mater. Sci. Proc. **74** (Suppl. 1), s86 (2002).
11. G. D. Bokuchava, A. M. Balagurov, V. V. Sumin, et al., J. Surf. Invest.: X-ray, Synchrotron Neutron Tech. **4**, 879 (2010).
12. T. Ungar and G. Tichy, Phys. Status Solidi A **171**, 425 (1999).
13. J. Pesicka, R. Kuzel, A. Dronhofer, et al., Acta Mater. **51**, 4847 (2003).
14. G. D. Bokuchava, I. V. Papushkin, V. V. Sumin, et al., Phys. Solid State **56**, 166 (2014).
15. G. D. Bokuchava, I. V. Papushkin, V. V. Sumin, et al., Phys. Part. Nucl. Lett. **10**, 157 (2013).
16. G. K. Williamson and R. E. Smallman, Philos. Mag. **1**, 34 (1956).
17. T. Ungar, I. Dragomir, A. Revesz, et al., J. Appl. Crystallogr. **32**, 992 (1999).
18. V. L. Arbuzov, G. A. Raspopova, and V. V. Sagaradze, Phys. Met. Metallogr. **108**, 77 (2009).
19. G. A. Raspopova and V. L. Arbuzov, Vopr. At. Nauki Tekh., Ser. Fiz. Rad. Povrezhd. Rad. Materialoved., No. 2, 14 (2009).

Translated by S. Rodikov